Metal–Water Interface Formation: Thermodynamics from Ab-Initio Molecular Dynamics Simulations

Fabiola Domínguez-Flores,[1, a)] Toni Kiljunen,[2] Axel Groß,[1] Sung Sakong,[1] and Marko M. Melander[2]
[1)]*Institute of Theoretical Chemistry, Ulm University, 89081 Ulm, Germany*
[2)]*Nanoscience Center, Department of Chemistry, University of Jyväskylä, P.O. Box 35 (YN), FI-40014 Jyväskylä, Finland*

(*Electronic mail: marko.m.melander@jyu.fi)

(*Electronic mail: sung.sakong@uni-ulm.de)

(Dated: 30 August 2024)

Metal–water interfaces are central to many electrochemical, (electro)catalytic, and materials science processes and systems. However, our current understanding of their thermodynamic properties is limited by the scarcity of accurate experimental and computational data and procedures. In this work, thermodynamic quantities for metal–water interface formation are computed for a range of FCC(111) surfaces (Pd, Pt, Au, Ag, Rh, and PdAu) through extensive density functional theory based molecular dynamics and the two-phase entropy model. We show that metal–water interface formation is thermodynamically favorable and that most metal surfaces studied in this work are completely wettable, i.e., have contact angles of zero. Interfacial water has higher entropy than bulk water due to the increased population of low-frequency translational modes. The entropic contributions also correlate with the orientational water density and the highest solvation entropies are observed for interfaces with a moderately ordered first water layer; the entropic contributions account for up to ca. 25 % of the formation free energy. Water adsorption energy correlates with the water orientation and structure, and is found to be a good descriptor of the internal energy part of the interface formation free energy but it alone cannot satisfactorily explain the interfacial thermodynamics; the interface formation is driven by the *competition* between energetic and entropic contributions. The obtained results and insight can be used to develop, parametrize, and benchmark theoretical and computational methods for studying metal–water interfaces. Overall, our study yields benchmark-quality data and fundamental insight into the thermodynamic forces driving metal–water interface formation.

Keywords: Electrochemistry, Solvation, Solid-Liquid Interfaces, Implicit solvent models, Thermodynamics

I. INTRODUCTION

Metal–water interfaces are pivotal for various applications in catalysis, materials science, and electrochemistry.[1–5] In electrocatalysis and electrochemistry, much of the current research is aimed at understanding how the aqueous metal interfaces or electrochemical double layers affect reaction kinetics and selectivity.[6,7] Given the role of the interface in determining reaction thermodynamics and kinetics of the system, it can even be said that the interface *is* the electrocatalyst.[8] However, our understanding of metal–water interfaces at the atomic scale is quite limited. In addition to the many open questions regarding the influence of interfacial water and ions on (electro)chemical reactions, even the basic thermodynamic properties of the interfaces remain deficient. For instance, it is generally unknown whether the formation of the interface is primarily driven by energetic or entropic factors and how each contribution depends on the electrolyte and the electrode material. It also remains largely unknown how the interfacial structure and dynamics are linked with its thermodynamic properties.[9,10]. The fundamental understanding of solid–liquid thermodynamics may have a crucial influence in the design of electrocatalytic systems, where the catalyst wetting[11] or the liquid entropy[12] may substantially impact activity and selectivity.

The main difficulty in understanding the thermodynamics of metal–water interfaces lies in the inherent complexity and heterogeneity at the sub-nanometer scale, which poses severe challenges to computational, theoretical, and experimental approaches. Although it is possible to directly measure interfacial thermodynamic quantities such as the surface tension and the contact angle, the solvation energies of metals have not been reported due to the difficulty of preparing smooth defect- and impurity-free surfaces. The experimentally measured quantities strongly depend on the sample quality and are available only for a handful of metal surfaces. While the low-temperature adsorption of water on metal surface is well-characterized,[13] the values of surface tension, work of adhesion, and contact angle measured at room temperature are scattered and even contradictory.[14–16] For instance, water contact angle measurements for the same material indicate either complete wetting (contact angle is zero) and strong hydrophilicity[17–19] or a partial wetting and hydrophobicity.[20] Although most studies seem to agree that water completely wets metal surfaces and that the contact angle is zero at room temperature, this only sets the lower limit for the work of adhesion that can be estimated from contact angle measurements. In particular, the Young-–Dupré equation that relates the work of adhesion (W_{ad}) and the liquid–vacuum surface tension (γ_{lv}) to the contact angle shows that the angle zero is reached when W_{ad} exceeds twice the γ_{lv}. Hence, the exper-

[a)]Previous affilition: Nanoscience Center, Department of Chemistry, University of Jyväskylä, P.O. Box 35 (YN), FI-40014 Jyväskylä, Finland

imental value[21] of 4.54 meV/Å^2 for the water–vacuum surface tension means that one cannot use contact angle measurements to extract thermodynamic quantities such as work of adhesion, metal–water surface tension, or the free energy of formation, for interfaces that interact strongly with water, i.e., when $W_{ad} > 9.1$ meV/Å^2.[22,23]

Only the recent meniscus measurements have successfully measured the absolute surface tensions and works of adhesion for Pt, Au, and Ag interfaces with water, showing that these surfaces are hydrophilic.[24] However, even the meniscus experiments were performed with macroscopic samples containing multiple surface orientations and possibly defects. The absence of pristine single-crystal experiments is the main obstacle to quantitatively match the experimental findings to the atomic-scale surface structures.

Electrochemical techniques provide alternative ways of measuring interfacial thermodynamic quantities through the relations between temperature, electrode potential, and capacitance. Mercury electrodes, in particular, allow the direct measurement of interfacial absolute entropies, surface tensions, excess free energies, and capacitances.[25,26] In other cases, and solid electrodes in particular, the obtained information is indirect because only differential quantities are available. Therefore, the typical observables are changes of the surface tension or in the entropy. For instance, several studies demonstrated the change of entropy as a function of surface charge by using the temperature dependence of the surface capacitance and the potential of zero charge (PZC).[25,27–30] Furthermore, the results of electrochemical measurements always depend on the electrolyte, and the extraction of pure metal–water thermodynamics is generally not possible without extrathermodynamic assumptions.[28]

While both explicit and implicit solvent models provide the means to study electrode-electrolyte interfaces at the atomic scale,[9,31–34] relating the solid–liquid interface structures with their thermodynamic properties poses a serious challenge.[9,10] Given that implicit solvent models are based on approximate free energy functionals[35] they can directly provide thermodynamic quantities. In practice, however, their accuracy depends very sensitively on the used method and its parameterization.[36,37] Several techniques are also available for computing the free energies of solid–liquid interface formation and surface tensions using explicit molecular dynamics (MD) simulations.[38] The most straightforward method to compute the surface tension consists of evaluating the free energy change with respect to the interfacial area, that is, $\gamma = (\partial F/\partial A)$.[39,40] The surface tension can also be calculated from Young's equation after estimating the droplet contact angle from a MD simulation.[41] Another way to compute the surface tension is to use its mechanical definition, which requires estimating the differences between the longitudinal and transversal pressures.[42] Also various thermodynamic integration schemes and free energy perturbation methods have been developed for computing various interfacial thermodynamic quantities.[39,43–45] Finally, the entropy can be directly computed by using the two-phase perturbation theory (2PT),[46,47] which relies on separation of translational, rotational, and vibrational degrees of freedom (DoF) and calculating the entropy of each DoF from their density of state (DoS) function obtained from relatively short, $\sim$20 ps,[48,49] MD trajectories.

Most of the above methods require extremely long trajectories and thorough phase sampling to yield converged thermodynamic quantities. Hence, most of the methods for computing interfacial entropies are practical only when performed with classical MD simulations rather than using *ab initio* or density functional theoretical (DFT) methods. Therefore, to our knowledge, information on water–metal entropy, free energy of formation, or surface tension at the *ab initio* quality is not available while studies on interfacial structure and capacitance are abundant.[50–56] In the absence of DFT-quality data, perhaps the most accurate computational data available on metal–water thermodynamics has been obtained by combining a quantum mechanical (QM) description of metal with classical molecular mechanics (MM) model of water. For example, QM/MM-MD simulations by Gim *et al.* have provided insight on formation energies and wetting as well as linking them to interfacial structures.[14,57] However, the MM force fields cannot properly describe interfacial electron transfer or the formation of metal–water covalent bonds.[52,58]. The discrepancies between QM/MM-MD and DFT-MD can already be seen in the structures of metal–water interfaces: while MM and QM/MM methods predict a single peak in the water distribution at the interface for all the metals considered[14,59], DFT-MD simulations predict significantly more nuanced and varying distributions ranging from strongly adsorbed water molecules to more free, bulk-like water, depending on the metal element.[52,60].

In this work, we have carried out an extensive DFT-MD thermodynamics study of metal–water interfaces. We report metal–water interfacial free energies, surface tensions, and works of adhesion for a range of FCC(111) surfaces. With the help of the 2PT model, our results explicitly account for the contributions of entropy. In addition, we establish correlations between the thermodynamic quantities, structural, and electronic properties of the metal–water interfaces studied. Our work provides detailed fundamental understanding of metal–water interface thermodynamics and establishes a DFT-level benchmark dataset that can be used to guide the development of empirical force fields and implicit solvent models.

II. NUMERICAL METHODS

The computational framework to obtain the free energies of formation consist of three parts. First, we performed DFT-MD simulations to obtain the trajectories of the atomic structures and the internal energies of the interfaces. Second, we calculated the entropy of each system using the 2PT method. Finally, we evaluated the free energy changes with respect to three different experimentally relevant reference systems corresponding to either metal–water surface tension, surface solvation energy, or work of adhesion measurements, as shown in Figure 1. In practice, the reference systems are bulk forms of both metal and water, the metallic surface and bulk for water, or the metal and water surfaces, respectively.

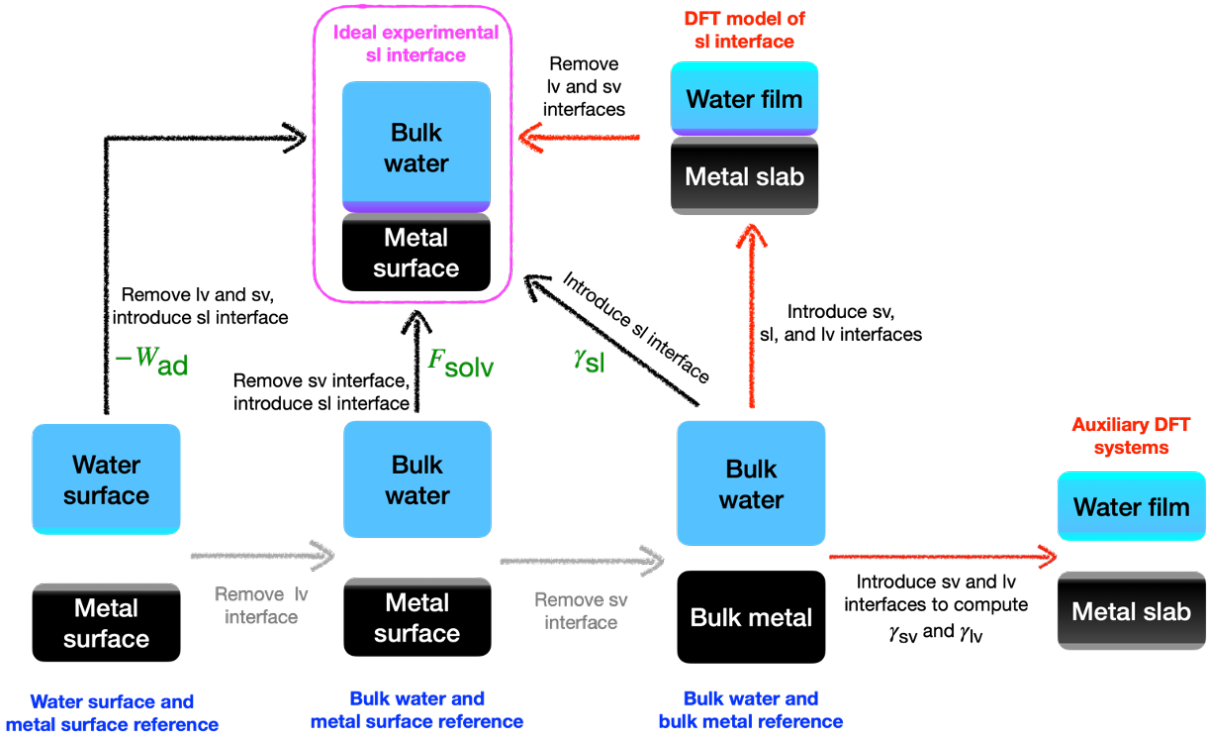

FIG. 1. Thermodynamic cycle used to assess the formation of solid–liquid interfaces and to illustrate the connections between different systems, references, and measurable quantities. The black arrows correspond to the route used in the present work and the equations defined in the SI. The grey arrows present an alternative route to connect the surface and bulk references. The red arrows show the DFT models of the sl, sv, and lv interfaces as well as their connections with the experimentally relevant systems. The highlighted (purple frame) system depicts the ideal experimental sl interface, which is our target of evaluation. The top right system corresponds to the DFT model of the sl interface used in the actual simulations. The bottom systems display the alternative reference schemes to obtain γ_{sl}, F_{solv}, or W_{ad}. The rightmost panel shows the auxiliary systems needed for closing the thermodynamic cycle. The different interfaces present in each system are colored as sl: purple, sv: grey, and lv: cyan.

A. DFT-MD simulations

We modelled the metal–water interfaces using a water film deposited on different metal surfaces. The metal parts consisted of five-layer-thick FCC(111) surface slabs modelled using a 6×6 unit cell. The water film consisted of 144 molecules, which amounts to ca. 20 Å thick film. The slab models were periodic in the xy-direction and 15 Å of vacuum was inserted in the z-direction to separate the periodic images from each other in this direction. We call this solid–liquid system as the sl model.[5,55,56,61] The reference model for water, called l, was computed as a bulk liquid using 96 water molecules in a simulation cell that corresponds to water density of 1 g/cm^3. The calculations regarding the bare 144-atom water film, corresponding to the liquid–vacuum interface system, are labelled by lv. Similarly, the reference systems for metal are labelled by s for the solid bulk and sv for the solid–vacuum interface system, i.e., the bare slab. The size of the solid bulk reference system s was set to $6 \times 6 \times 6$ atoms. During the DFT-MD simulations, two layers forming the base of the metal slab were immobilized at their optimized bulk positions. Therefore, we also evaluated the energies of unrelaxed s and sv models to obtain reference energies corresponding to the immobilized parts of the systems (see SI Equations (S4)–(S5) for details).

All the DFT-MD simulations were performed using the Vienna Ab initio Simulation Package (VASP).[62–65] The one electron bands were expanded in a plane wave basis with a cutoff energy of 400 eV. The electronic cores were described by the projector augmented wave (PAW) method.[66] The energy convergence criterion was set to 10^{-6} eV. To accurately model both the metal and the liquid systems[61,67–69] the exchange-correlation energies were evaluated using the revised Perdew-Burke-Ernzerhof (RPBE) functional[70] with the semi-empirical D3 dispersion correction scheme of Grimme using the zero-damping function.[71,72] The pair-interaction cutoff radius of the D3 correction was set to 10 Å. The dispersion correction for all metal atoms below the first layer was excluded since the screening of the van der Waals interactions in bulk metals is not correctly described in dispersion correction schemes.[68,73,74] The spurious dipole interactions between periodic images were removed by using the dipole correction in the z-direction. Due to the large unit cell sizes, only the Γ point was used for the k-point sampling in the simulations of interface, slab, and bulk models. However, to obtain the lattice constant for each metal, the optimizations were performed using a single atom in its FCC bulk geometry and using a fine k-point grid of $21 \times 21 \times 21$.

The DFT-MD simulations were performed within the canonical NVT ensemble at 298 K using the Langevin thermostat with a friction coefficient of 5 ps^{-1}. The Langevin thermostat is recommended for uniform kinetic energy distribution over all degrees of freedom.[75] However, the friction coefficient may impact the velocity auto-correlation functions and thereby the density of states distributions[76] and entropy values computed from them. We selected the friction coefficient to provide both good temperature control and minimal change of the DoS. Each system was first thermalized at least for 5 ps, whereas the lengths of the subsequent statistical sampling runs were 40 ps for the interfaces (sl), 20 ps for the bulk water (l), 11 ps for the water film (lv), and 5 ps for reference metal systems (s and sv). Based on the previous studies,[48,49] these sampling times are long enough for converged 2PT entropies within ± 1 J K^{-1} mol^{-1}. Our thorough convergence study (Supplementary Material Section S6) also shows that the internal energies, entropies, and free energies are well-converged and have uncertainties of $\pm$ 2 meV/Å^2, $\pm$ 0.01 meV K^{-1}, and $\pm$ 2 meV/Å^2, respectively. The employed setup gives a liquid–vacuum surface tension of 71.5 dyn cm^{-1} in excellent agreement with experiments (72.8 dyn cm^{-1})[21] thus providing a robust benchmark for the chosen approach and used parameters.

B. Analyzing the interfacial structure

We quantify the average water structures using the time-averaged planar density distributions in the z-direction using

$$\rho(z) = \frac{\rho_{\text{bulk}}}{A} \left\langle \sum_{l=1}^{n_l} \delta(z - z_l) \right\rangle , \tag{1}$$

where z is the distance from the metal surface, A is the surface area, l counts the water molecules, δ is the Dirac delta-function, and ρ_{bulk} is the bulk density of water. The distribution of water orientation with respect to the metal surface was computed as

$$\langle \theta(z) \rangle = \int_0^{\pi} \mathrm{d}\theta \, \theta P(\theta, z) , \tag{2}$$

where θ was defined as the angle between the bisector (dipole-orientation) of the water molecule and the reverse surface normal. $P(\theta, z)$ is the probability distribution function of observing that angle at z. The orientational water density was then defined as

$$\hat{\rho} = \rho(z) \cos \langle \theta(z) \rangle . \tag{3}$$

To quantify the average number of hydrogen bonds between water molecules in the trajectories, a similar procedure as in Eq. (1) was employed. The criteria for hydrogen bond identification were set as follows: the distance between two oxygen atoms of individual water molecules was $r_{\text{O-O}} < 3$ Å and the angle between an OH bond and an O atom in another molecule was $\angle_{\text{HOO}} < 30°$.

C. Free energy calculations

The Helmholtz free energies F were calculated directly by the definition

$$F(T) = \langle E(T) \rangle - T \langle S(T) \rangle , \tag{4}$$

where $F(T)$ is the canonical free energy at temperature T, and $\langle E(T) \rangle$ and $\langle S(T) \rangle$ denote the expectation values of the internal energy and the total entropy, respectively, of the systems. The expectation values were obtained as time averages over the DFT-MD trajectories.

The total entropies were evaluated within the 2PT method[46,77,78] from the DFT-MD trajectories using the DoSPT code by Caro et al.[79] In brief, the 2PT method computes the entropy in three steps: 1) splitting the DFT-MD trajectory dynamics into vibrational, rotational, and translational degrees of freedom (DoF), 2) computing the DoS functions for each DoF from the velocity auto-correlation functions, and 3) computing the total entropy as a sum of the three modes obtained using a weighted integral over the DoS of the corresponding DoF.[46,77] While originally developed for liquids[77,80,81], the 2PT formalism can also be applied to solid–liquid systems without issues.[82–84] Here we customized the use of the DoSPT code from tetragonal to monoclinic simulation cells. In the interfacial systems, the entropy can further be divided into metal and water contributions by defining the so called supergroups in the DoSPT program. To decompose even further, we partitioned the entropy of water into interface and bulk-like regions according to the distance of the molecules from the metal surface.

Our primary goal was to compute various thermodynamic quantities related to the formation of the solid–liquid interface. This was achieved by following the thermodynamic cycle, shown in Figure 1, which relates the needed total free energies (F), free energy changes (ΔF), and surface tensions ($\gamma = \Delta F / A$). The primary quantities of interest were the area-normalized free energy of formation of the solid–liquid interface ($\Delta F_{\text{sl}} / A_{\text{sl}} = \gamma_{\text{sl}}$), the free energy of solvation of the metal surface (F_{solv}), and the work of adhesion (W_{ad}). Figure 1 demonstrates how the free energy of bulk solid metal F_{s} and that of the bulk water F_{l} can be used as the references for γ_{sl}. Similarly, for F_{solv}, the reference states are the metal surface in vacuum and the bulk water with the free energies of F_{sv} and F_{l}, respectively. W_{ad} is obtained by referencing against the metal–vacuum and water–vacuum surfaces. Here, we give a general description of the methodology while the detailed working equations used in the present work are provided in the Supplementary material (SM), Section S1 and Equations S1-S9.

To compute γ_{sl}, F_{solv}, and W_{ad}, the free energies of formation of the liquid–vacuum and solid–vacuum interfaces were needed as these were present in our finite DFT model setups. To obtain the thermodynamic quantities for our target system, the experimental solid–liquid interface alone, these contributions need to be removed surface solvation (F_{solv}) and metal–water interface (γ_{sl}) free energies as well as the work of adhesion (W_{ad}). This was accomplished by computing the free energies F_{lv} and F_{sv} and the corresponding surface tensions

γ_{lv} and γ_{sv}. An additional complication for such referencing arises due to the frozen base layers of the metal slabs, which required appropriate treatment detailed in SM, Equations (S4)-(S5).

D. Interfacial thermodynamics from DFT-MD simulations

The differential quantities are always computed with respect to some well-defined reference state, which is specified by the choice of the corresponding chemical potentials μ. By working within an "ab initio thermodynamics" framework,[34] the free energy change is

$$\Delta F_{\mathrm{i}} = F_{\mathrm{i}} - \sum_{\mathrm{j}} n_{\mathrm{j}}\,\mu_{\mathrm{j}}\,, \tag{5}$$

where i is the interfacial system of interest (sl, sv, or lv), j correspond to the references (sv, lv, s, or l), and n_{j} is the number of atoms or molecules in the corresponding system. Thus, the chemical potentials are considered as free energies per component j by $\mu_{\mathrm{j}} = F_{\mathrm{j}}(n)/n$. In case the reference state itself contains an interface of area A_{i}, the free energy can be endowed with a surface work term such that the chemical potential assumes the form $\mu_{\mathrm{j}} = (F_{\mathrm{j}}^{\mathrm{bulk}}(n) + \gamma_{\mathrm{j}} A_{\mathrm{i}})/n$. The adsorption energy of a single water molecule can be obtained by reducing Eq. (5) to $\Delta E_{\mathrm{ads}} = E_{\mathrm{slab+H_2O}} - E_{\mathrm{slab}} - E_{\mathrm{H_2O}}$, where the terms represent the total energy of the the slab with an adsorbed water molecule, energy of the bare slab, and energy of a gas-phase water molecule, respectively.

Interfacial quantities are more meaningful and comparable when normalized by the surface area, which directly leads to surface tensions. The different surface tensions can generally be calculated as

$$\gamma_{\mathrm{i}} = \frac{\Delta F_{\mathrm{i}}}{A_{\mathrm{i}}}\,. \tag{6}$$

The required total free energies F_{sl}, F_{sv}, F_{s}, F_{lv}, and F_{l}, were calculated using Eq. (4). These values were then used for computing the free energy changes. According to Eq. (5), the free energy of formation of the liquid–vacuum interface is given by

$$\Delta F_{\mathrm{lv}} = F_{\mathrm{lv}} - n_{\mathrm{l}}\,\mu_{\mathrm{l}}\,, \tag{7}$$

where n_{l} is the number of water molecules, $\mu_{\mathrm{l}} = F_{\mathrm{l}}(n)/n$ is the water chemical potential, and the free energy of vacuum is zero. The water–vacuum surface tension was calculated using the auxiliary lv reference system and the equation

$$\gamma_{\mathrm{lv}} = \frac{\Delta F_{\mathrm{lv}}}{2A_{\mathrm{lv}}}\,, \tag{8}$$

where the factor two is included because the water film has a vacuum interface on both sides. Equivalent definitions apply for the formation of solid–vacuum interfaces ΔF_{sv} and surface tensions γ_{sv}. The metal–water surface tension, characterizing the formation free energy of the sl interface from the bulk metal and water phases, is given by

$$\gamma_{\mathrm{sl}} = \frac{F_{\mathrm{sl}} - (F_{\mathrm{s}} + F_{\mathrm{l}})}{A_{\mathrm{sl}}} - \gamma_{\mathrm{lv}} - \gamma_{\mathrm{sv}}\,, \tag{9}$$

where bulk references are used. Alternatively, using the bulk reference for the liquid only and maintaining the bare slab as the reference for metal, the surface-normalized free energy of solvation was calculated as

$$F_{\mathrm{solv}} = \frac{F_{\mathrm{sl}} - (F_{\mathrm{sv}} + F_{\mathrm{l}})}{A_{\mathrm{sl}}} - \gamma_{\mathrm{lv}}\,. \tag{10}$$

The resulting $\gamma_{\mathrm{sl}} > 0$ as otherwise the bulk phases would spontaneously decompose to maximize the interfacial area. On the other hand, F_{solv} can be either negative or positive as it measures the effective solvation energy of the metal surface per unit area. Note that F_{solv} measures the surface–water interaction only and does not directly tell whether a surface is wetting or not because the contact angle (Eq. (11b)) depends also on the properties of the water–vacuum and metal-vacuum interfaces.

The free energies and surface tensions can be used to calculate various experimental observables. For instance, the surface tensions are used in the Young–Dupré equation to compute the work of adhesion (W_{ad}) and the contact angle (θ_{sl}):

$$W_{\mathrm{ad}} = \gamma_{\mathrm{lv}} + \gamma_{\mathrm{sv}} - \gamma_{\mathrm{sl}}\,, \tag{11a}$$

$$\cos(\theta_{\mathrm{sl}}) = \frac{W_{\mathrm{ad}}}{\gamma_{\mathrm{lv}}} - 1\,. \tag{11b}$$

As shown in Equations (S8)-(S9), the adhesion work can also be computed directly from the simulated free energies. It should be noted that the accuracy of W_{ad} depends not only on the solid–liquid and liquid–vacuum surface tensions but also on the solid–vacuum surface tensions. The accuracy of γ_{sv} depends on the computational method used. For example, GGA functionals are known to underestimate γ_{sv}, which may cause an overestimation of the hydrophilicity.[85,86]

We also separately considered the contributions of (internal) energy ($E(T)$) and entropy ($S(T)$). The entropy contribution to the surface tension is defined as

$$\Delta\gamma_{\mathrm{sl}}(S) = \gamma_{\mathrm{sl}}(E) - \gamma_{\mathrm{sl}}(F)\,, \tag{12}$$

where $\gamma_{\mathrm{sl}}(E)$ is the energetic version of the surface tension computed from Eq. (6) but neglecting the entropy contributions of Eq. (4) throughout.

We have also used the flexibility of DoSPT to separately study the entropy of the first water layer (1WL) close to the metal surface as well as the entropy of the other water molecules comprising the interfacial bulk-like water layer (IBL), see the rough illustration in Figure 2. The division was made based on the $\rho(z)$ structure. More precisely, the 1WL was defined as the region between the metal surface at $z = 0$ and the dip in $\rho(z)$ at $z \approx 4$ Å after the first density peak for Au and Ag and after the second peak for Pd, Pt, and Rh. Hence, the 1WL corresponds to an interfacial region where the water molecules have a preferential orientation and higher density as compared to bulk water. The IBL was considered to extend from the dip up to the onset of the lv interface (at $z \approx 15$ Å), which was estimated by fitting a Gaussian function to the tail

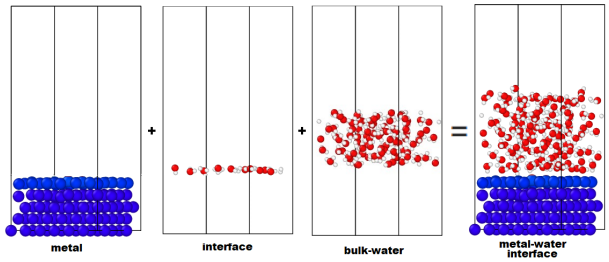

FIG. 2. Graphical representation of the water partition into first interfacial water (bi-)layer (1WL) and interfacial bulk water layer (IBL) contributions.

of $\rho(z)$ and considering only those water molecules that were at least one full-width at half maximum (FWHM) distance away from the fit function center value. Because the water molecules are free to exchange positions between 1WL, IBL, and vapor regions, the division of molecules to these groups is not unique and only qualitative analysis of the entropy was possible. To this end, we chose to track which molecules were located within the 1WL and IBL for more than 80 % of the simulation time, and computed the 1WL and IBL entropies accordingly. The influence of the residence percentage on the entropies was preliminarily checked, and we observed that the 50–80 % criterion lead to very similar interfacial entropies. For details, see Supplementary material Table S1.

III. RESULTS

A. Water structure near metallic surfaces

The distribution profiles $\rho(z)$ and orientation of water molecules at the metal surfaces are presented in Figure 3. The Au and Ag feature only a single broad $\rho(z)$ peak at ca. 3 Å from the surface. The other metals generate a doublet peak with maxima at ca. 2 and 3 Å corresponding to a more ordered water structure in the first layer. Going from Au to Rh, the density dip that defines the 1WL region boundary shifts slightly inwards, from 5 Å to 4.5 Å indicating a stronger interaction between Rh and water. As shown in Figure S2, the more structured interfacial water layer also leads to more pronounced oscillations in the electrostatic potential. In general, the obtained structures are similar and in agreement with the previous DFT-MD[51] and experimental results[87].

The central and bottom panels in Figure 3 show that the water orientations depend on the metal. The density-weighted orientational distribution, $\rho\langle\cos\theta\rangle$, shows that on Rh, Pt, Pd, and Ag the closest water molecules are preferentially oriented with $\langle\theta\rangle \approx 120^\circ$ corresponding to O–H pointing away from the surface. On Au water does not have a preferential orientation. The outer maximum of the resolved $\rho(z)$ doublet in Pd, Pt, and Rh coincides with orientations of $\langle\theta\rangle = 70^\circ$–$75^\circ$ from tilted molecules. Interestingly, the middle panel in Figure 3 displays a rather similar trend of water orientation for all the metal surfaces, i.e., the metal type does not affect the averaged water configuration at a distance from the surface. However,

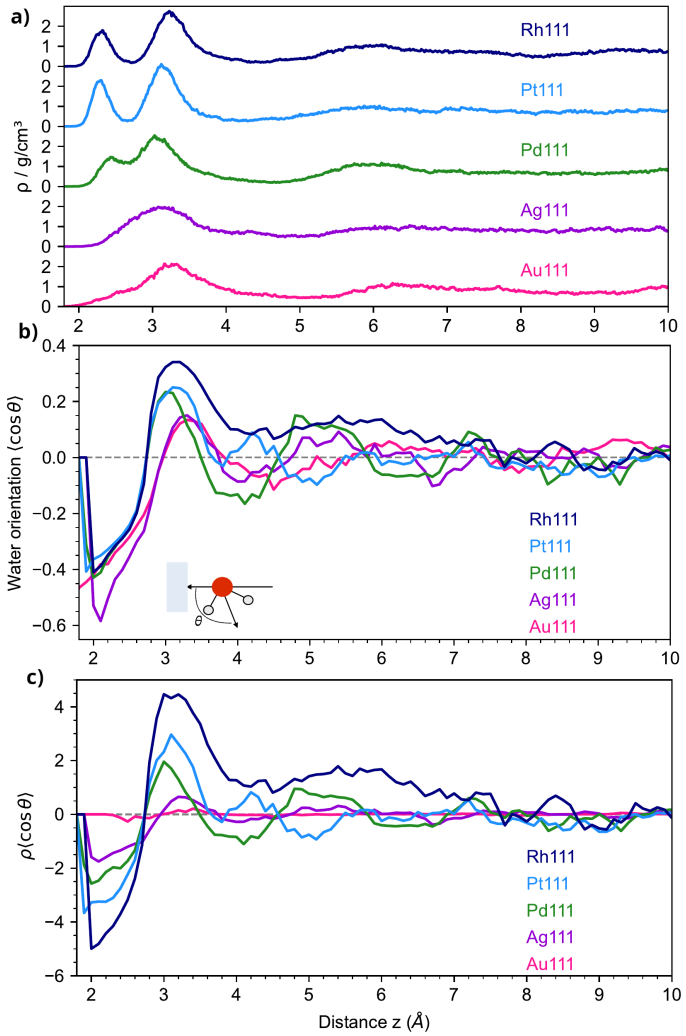

FIG. 3. Water structure profiles as a function of distance from the metal surface. a): averaged density distribution, b): averaged water bisector (dipole) orientation, c): averaged orientational density.

the abundance of the water and hence the orientational density depend strongly on the metal–water interaction strength, as discussed in Section "Analyzing interfacial metal–water thermodynamics".

In most cases, the water molecules retain their molecular structure and do not dissociate during the DFT-MD simulations. On Rh, however, a spontaneous dissociation to H_3O^+ and OH^- was observed. The charge analysis (see Supplementary material, Figure S2) showed that the dissociation is due to the charge polarization at the interface as an electron transfer event from the water to the Rh surface was observed. The electron transfer effectively removes one electron from the water film which was followed by autoionization of a water molecule and emergence of a neutral OH fragment and a proton in water. As the computed potential of zero for the Pd(111) is in a good agreement with the experimental value (see Figure S5), the simulated systems with one OH fragment is expected to be a good model for the Rh(111)–water interface.

In addition to the spatial and orientational densities of water, the interfacial hydrogen bonding also varies as a function of the distance from the metal. Figure 4 maps the number of hydrogen bond donors[51] and shows that the water molecules within the 1WL assemble into a network with a dual nature. First, at $z \sim 2$ Å from the metal surfaces, there are more hydrogen-bonded molecules than in the bulk region ($z \gtrsim 9$ Å), while at $z \sim 3$ Å the number of hydrogen bonds dips below the bulk value. Thus, the oscillation reflects the bilayer-type $\langle \cos\theta \rangle$ distribution in Figure 3. Quantitatively, in the peak (dip) region the water molecules donate 1.50–1.75 (0.50–0.75) hydrogen bonds in average depending on the metal. Inspection of the distribution shows that at Au and Pt interfaces, water has the highest peak number of hydrogen bonds while Rh has the lowest dip below the bulk value.

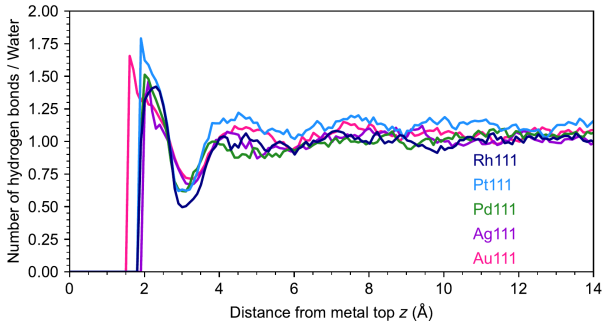

FIG. 4. The average number of hydrogen bonds donated by a water molecule as a function of distance from the metal surfaces.

B. Decomposed Density of States Analysis

The decomposed density of states for the entire water film on different metals as obtained by the DoSPT program are shown in Figure 5. Since the studied water films have two interfaces, one with the metal and another with the vacuum, the changes with respect to bulk DoS occur on both sides. The translational bulk frequencies correspond to the skewed Gaussian band that peaks at around 50 cm^{-1}, while the rotational motions lead to the broad Gaussian type band centered at around 500 cm^{-1}. The rotational contributions to the DoS on the metal surfaces are rather independent of the presence of the metal substrate and are nearly indistinguishable from those of bulk water. Because the high-frequency stretching and bending modes are also close to their bulk liquid properties (shown in Figure S1), here we focus on the translational modes only.

As previously identified by Gim *et al.*,[88] bulk liquid water exhibits two overlapping DoS bands for the translational modes. The bands arise from the collective dynamics of the water molecules interconnected through hydrogen bonds, i.e., the major peak $\tilde{\nu}_{OOO}$ around 50 cm^{-1} corresponds to intermolecular O–O–O motions while the lower-intensity peak $\tilde{\nu}_{OO}$ around 200 cm^{-1} is due to intermolecular O–O stretching. In general, the water films on all metals exhibit a higher DoS peak intensity for the $\tilde{\nu}_{OOO}$ motion than bulk water does

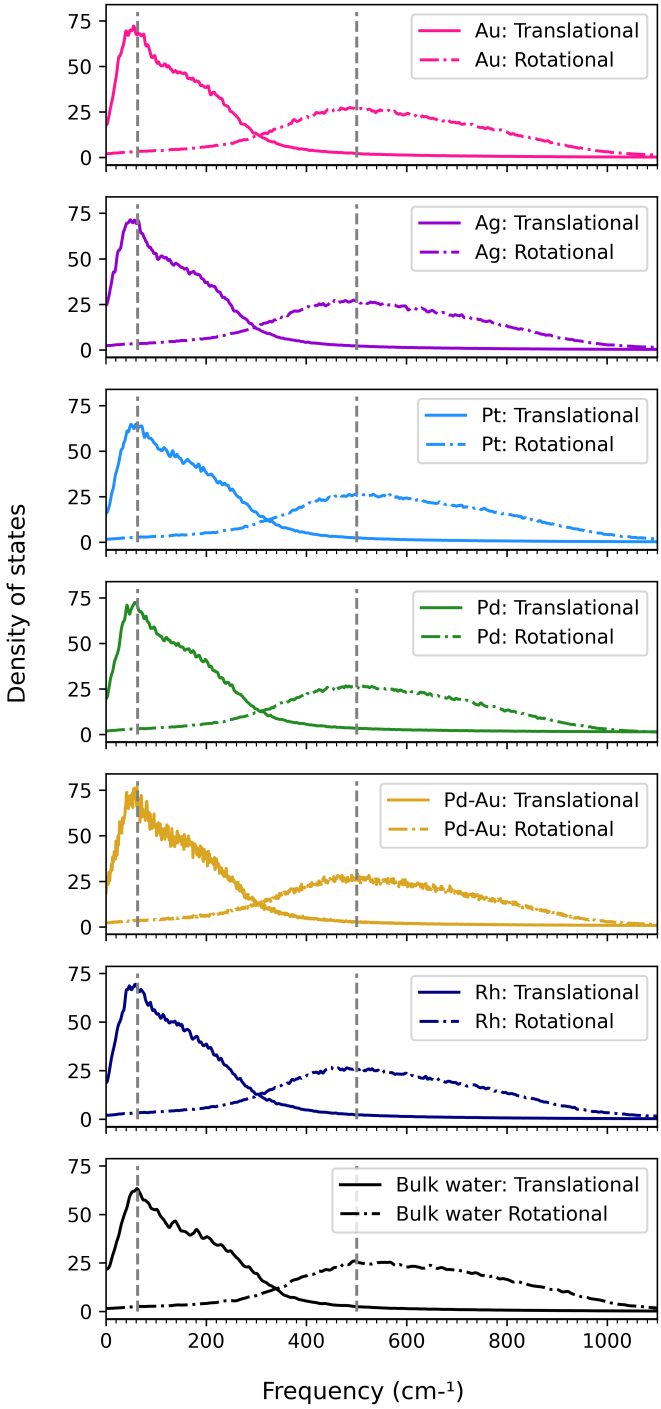

FIG. 5. Density of states (DoS) plot of translational (solid line) and rotational (dash-dotted line) degrees of freedom for the water films on Au(111), Ag(111), Pt(111), Pd(111), Pd/Au(111), and Rh(111) surfaces, and for bulk water. The bulk DoS is normalized by the number of water molecules (144) in the metal–water systems.

while the $\tilde{\nu}_{OO}$ motion is very similar across all the studied systems. This means that a water film on a metal surface has more O–O–O torsional than O–O stretching modes as compared to bulk water. The increased torsional motions are due to the water molecules at liquid–vacuum interfaces, where molecules drift more freely into the vacuum region.

While the total DoS distribution of the entire water film is rather similar across all the studied systems, the DoS for the first interfacial water layer (1WL) does depend on the underlying metal, as shown in Figure 6. The rotational DoS of the 1WL depends only slightly on the presence or the nature of the metal surface while the translation part is more sensitive. As the rotational frequencies remain unaffected, the rotational reorganization dynamics at the interface are also independent of the metal surface. For Au and Ag, the translational frequency retains its bulk value, while on Pt, Pd, and Rh, the band shifts to higher frequencies because of the higher local water density below 3 Å from the metal surface. Since the higher frequencies correspond to shorter velocity autocorrelation times, shifts in the DoS towards higher translational frequencies indicate faster translational reorganization of the interfacial water layer.

The translational DoS of the 1WL slightly differ from the bulk water by the shape and maximum position while the maximum intensity is largely unaffected. In particular, the two bands corresponding to intermolecular O–O–O and O–O motions in bulk water cannot be distinguished at the interfaces, where only a single broad band is observed. Figure 6 shows that on Au the translation peak maximum is slightly shifted to lower frequencies while on Ag the peak position remains unchanged as compared to bulk water. On Pd, Pt, and Rh the translational peak is shifted to slightly higher frequencies when compared to bulk water.

The broadened peaks and shifts in the maxima can result from various changes in the the O–O–O or O–O dynamics, which can be addressed by analyzing differences between the 1WL and bulk water DoS. The overlain DoS in Figure S3 shows that the translational maximum shifts to a lower frequency while the DoS in the region between the O–O–O and O–O frequencies increases on Au surface. The lower maximum frequency indicates that the torsional O–O–O interactions are weakened by the surface. Combining this with the coalescence of the O–O–O and O–O peaks indicates that also the O–O frequency distribution becomes skewed towards lower frequencies. Together these observations mean that on gold the average O–O–O and O–O interactions are slightly weaker than in bulk water and that the interfacial water would be looser and less organized than bulk water. On Ag, the O–O–O peak maximum is not affected by the surface but the O–O peak is shifted towards a lower frequency. These observations suggest that on silver the long-range interactions and ordering remain unaffected while the O–O interactions are slightly weakened and the 1WL would have less short-range ordering. On Pt, Pd, and Rh the shift in the peak maximum towards higher frequencies indicates stronger O–O–O interactions and increased long-range ordering. However, on Pd the O–O intensity is skewed towards lower frequencies, on Pt the O–O frequencies are slightly skewed towards higher frequencies while on Rh the O–O region is rather unchanged as compared to bulk water. These findings indicate that 1WL on Pd has less O–O correlation and hence less short-range order, on Pt the O–O interaction is slightly stronger while on Rh the short-range order does not not deviate from bulk water.

The 1WL DoS can also be understood by correlating it with the the average water structure on the surface. In particular, in the first high-density water region on Pt, Pd, and Rh ($\sim$ 2 Å, Figure 3) the metal–water molecule angle $\theta \sim 120^\circ$. In this region, number of hydrogen bonds donated by a water molecule is higher than in bulk water (Figure 4). Together these factors lead to an increased O–O–O DoS and indicate a rigid interfacial water in the first high-density water region on Pt, Pd, and Rh. In the second high-density region ($\sim$ 3 Å, Figure 3) the metal–water angle $\theta \sim 70^\circ$–75° for Rh, Pd, and Pt while Ag and Au do not notably prefer any water orientation. The number of hydrogen bonds made by a water molecule on all the studied metal surface is lower than in bulk water. Only on Au and Ag the total DoS in the O–O region is slightly more populated than in bulk water which would indicate a slightly increased short-range water structure on these metals when combined with the structural information. However, correlations between the structure and DoS in the second high density region cannot be readily identified.

Additional insight into the water dynamics can be gained by using the linear correlation between the DoS at zero frequency and the water diffusion constant.[47] The DoS at 0 cm^{-1} (Figure S3) shows that the water diffusion within the 1WL on Au and Ag is similar to that in bulk water while on Pd, Pt, and Rh the water diffuses slightly slower. A similar trend holds for the entire water film, as shown in Figure **??**. The translational DoS of water molecules within the 1WL can tentatively be understood by considering the four water diffusion mechanisms and barriers on different surfaces as suggested by Fang et al.:[89] on Ag, water diffusion takes place through dimer translations with a barrier of 0.05 eV; on Pt, monomer translation has the lowest barrier of 0.18 eV; on Rh, a water exchange dominates the diffusion with a barrier of 0.1 eV; on Pd, all diffusion mechanisms have a barrier of 0.1 eV.[89] In particular, monomer and dimer diffusion lead to total water displacements, but rotation and site exchange do not, which impacts both the diffusion constant and the correlated motion of the water molecules. Pt has the slowest water surface diffusion due to the higher barrier and single molecule translations. Water is most diffusive on Ag due to the low energy barrier and concerted motion of several water molecules. Pd presents an intermediate case with modest energy barriers and various diffusion pathways. Overall, the surface diffusion mechanisms and barriers qualitatively explain the interfacial part of the translational DoS on different metals.

The right-hand-side panel of Figure 6 shows the vibrational modes of water on the metal surfaces and in bulk. The narrow band of the water bending mode is shifted to a lower frequency from the bulk value of ca. 1700 cm^{-1} on Pd, Pt, and Rh, where the water density distribution $\rho(z)$ shows two peaks at the interface region. Since the bending mode doesn't couple strongly to the movement of other water molecules, the frequency decrease reflects softer intramolecular bonds, which

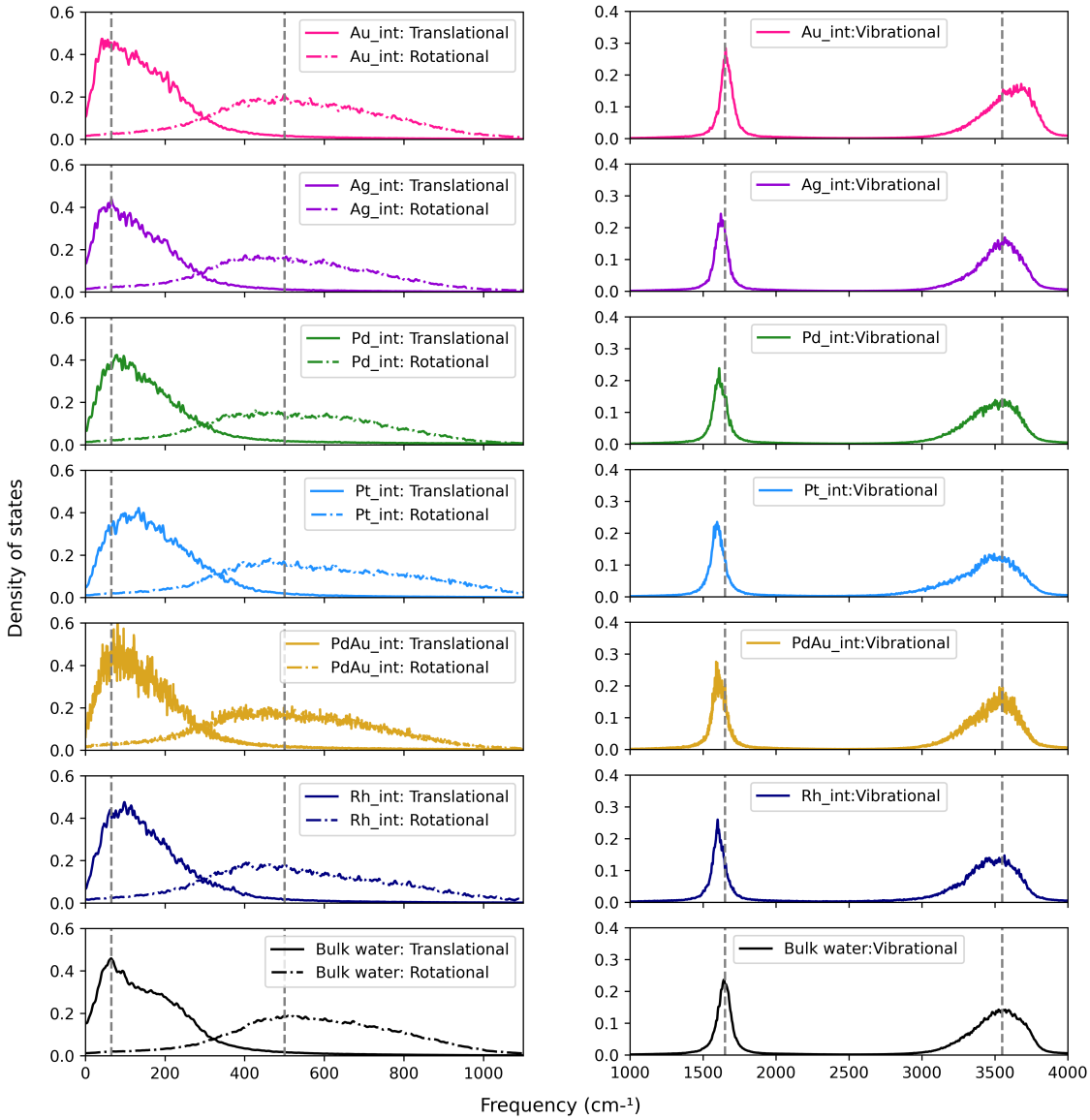

FIG. 6. DoS for the first interfacial water layer (1WL) on different FCC(111) surfaces compared to bulk water. Because the number of water molecules within the 1WL is different for different surfaces, the DoS are normalized by the number of molecules within the 1WL of each surface.

is likely caused by partial charge transfer from adsorbed water molecules to the surface. The O–H stretching mode around 3500 cm^{-1} in the bulk liquid phase is rather broad due to the dynamic forming and breaking of the hydrogen bonds. The small red-shift of the stretching mode on Pd, Pt, and Rh indicates softer O–H bonding at these surfaces. On Ag, both vibrational modes are relatively close to their bulk liquid counterparts. On Au, however, the surface seems to induce a blue-shift in the stretching mode while the bending mode remains at the bulk position. The blue-shift is peculiar since the Au–water has the weakest chemisorption and it would be expected that the DoS were then more bulk-like, similar to the Ag case. The apparent blue-shift may result if a hydrogen-bonding related broadening mechanism is effectively suppressed. We suggest that the blue-shift of the stretching mode indicates a weaker or looser hydrogen bond network at the Au–water interface.

C. Thermodynamics of metal–water interfaces

The computed thermodynamic quantities for metal–water interface formation are listed in Table I. Overall, the entropy of water molecules in the water film is increased compared to the calculated bulk value of 0.55 meV/K. This is due to the increased DoS at the low-frequency range as shown in Figure 6. All the studied interfaces have positive free energies of formation with respect to the bulk references; correspond-

ingly, $\gamma_{sl}(F) > 0$. Rh and Pt exhibit the highest surface tensions, Pd and Pd-Au have intermediate values similar to each other, while Au and Ag form the pair of lowest values. The same energetic ordering is observed for $\gamma_{sl}(E)$. As both $\gamma_{sl}(E)$ and $\gamma_{sl}(F)$ contain energetic contributions from the cleavage as well as solvation of a metal surface, a good correlation between them and the solid–vacuum interfacial energies[90] is expected and observed; the metals with the highest γ_{sv} also have the highest γ_{sl}. The data also show that the magnitude of the entropy of the interface formation varies from one metal to another. For instance, on Pd the entropy contribution to $\gamma_{sl}(F)$ is about 25 % of the total free energy while on Rh and Pt the entropy contribution is less than 3 %. For Au and Ag the entropy contributions to the surface tension are about 7 % and 15 %, respectively.

Direct thermodynamic measures for forming the metal–water interface from a metal and a water surface or from a metal surface and bulk water are given by the work of adhesion (W_{ad}) or the free energy of surface solvation (F_{solv}), respectively. These measures show that Pd is the most strongly solvated surface, followed by Pt and Rh, and then by Pd-Au, Ag, and Au. Note that the ordering between γ_{sl} and W_{ad} or F_{solv} depends on the used reference system. Most of the metal surfaces are also hydrophilic and completely wetting as the contact angles are 0°. Ag and Au are the only exceptions with contact angles 52° and 95°, respectively. The predicted works of adhesion are in a decently satisfactory agreement with those measured using the meniscus technique:[24] the calculated (measured) W_{ad} in meV/Å^2 are 4.06 (15.92) for Au, 7.23 (15.56) for Ag, and 20.49 (15.9) for Pt. This comparison shows that the calculated and experimental values are of similar magnitude but the experimental data indicates that all surfaces are completely wetting while the simulations predict that water would not completely wet the Ag and Au surfaces. The qualitative disagreement between the computational and experimental results for Ag and Au is attributed to the different surface structures and morphologies in the simulations and experiments; we used ideal FCC(111) surfaces while the meniscus experiments used macroscopic samples without controlling the surface orientations or presence of defects. It is well-known that more open surfaces exhibit stronger metal–water interactions[13] and are thereby more wettable.

Our results for the work of adhesion and contact angle differ significantly from the QM/MM results reported by Gim *et al.*[14] who predicted that Ag and Au would have much stronger water adhesion and contact angles of zero. We should also note that their water distribution functions are quite different from ours. The QM/MM simulations predict the water distribution on Ag and Au to be very similar to that on Pd and Pt while our results in Figure 3 show that both the water density and orientation of Ag and Au are drastically different from those of Pd and Pt; the QM/MM simulations do not capture the water adsorption peak on Pd and Pt but still predict a high interfacial water concentration. While the adsorption energies of a water molecule reported by Gim *et al.* are similar to ours, we suppose that the differences in the water structure are likely due to the use of just a single water orientation in the QM/MM parameterization.[14]

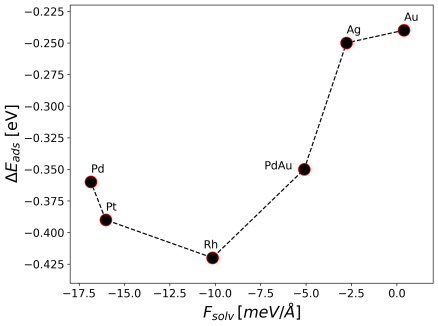

FIG. 7. Adsorption energy of a water molecule ΔE_{ads} as a function of the free energy of solvation F_{solv}.

D. Analyzing interfacial metal–water thermodynamics

Our results show that the thermodynamics of surface solvation is driven by both energetic and entropic contributions, that is, the energy of a given configuration and the probability of its occurrence. The competition between these two contributions can be understood by correlating the thermodynamic quantities and the adsorption energy of a single water molecule. Figure 7 shows that water adsorption is strongest for Rh, but its F_{solv} is modest compared to Pd and Pt that exhibit weaker water adsorption. The interfacial solvation energy is reduced for the more weakly binding metals Ag and Au, which on the other hand have higher or similar entropy contributions to the surface tension as Rh. Compared to Rh, the solvation of Pd and Pt surfaces is more exergonic but the Pd–water interface formation is more entropy-driven while Pt-water has a smaller entropy contribution. These results show that the interface thermodynamics depends sensitively on both the energetic and entropic contributions; while strong binding is usually beneficial for wetting, too strong binding suppresses the entropic contributions.

Since the main contribution to entropy arises from the low-frequency translational and rotational modes, we focus on these modes only. The DoS features for water shown in Figures 5 and 6 were discussed above. Also here, we quantify the corresponding entropy by separately examining the metal surface, 1WL, and IBL contributions (see Figure 2). The entropies of water components are collected in Table II such that the water molecules which stay in the 1WL region for 80 % of the simulation time are included as the 1WL contribution. The number of such molecules in the simulation box was of the order of 20. While the chosen residence time impacts the absolute local entropy values (see Table S1), the trends of the absolute 1WL and IBL entropies are robust enough for a qualitative discussion.

The first observation is that the water entropy in both 1WL and IBL is larger than in the bulk water (0.55 meV/K per water molecule). This is due to the more pronounced translational contributions at the interface as shown in Figures 5 and 6. Au and Ag have the highest 1WL entropies, which likely results from the relatively unorganized water structure (Figure 3) and high water diffusivity[89] in the 1WL. Pd-Au and Pt

TABLE I. Computed thermodynamic quantities for the metal–water interfaces. γ_{sv} is the solid–vacuum surface tension based on the free energy. S_{H_2O} is the average entropy per water molecule in the sl model. $\gamma_{sl}(E)$ and $\gamma_{sl}(F)$ are the solid–liquid surface tensions based on the internal energy and free energy, respectively. $\Delta\gamma_{sl}(S)$ is the entropic contribution to the surface tension computed using Eq. (12). W_{ad} is the work of adhesion by Eq. (11), F_{solv} is the free energy of surface solvation referenced against bulk water and the metal surface by Eq. (10), and θ_{sl} is the metal–water contact angle. The units are meV/K for the S_{H_2O} and meV/Å^2 for the γ_i at 298 K. The contact angles θ_{sl} are given in degrees. The liquid–vacuum surface tension is $\gamma_{lv} = 4.46$ meV/Å^2. The uncertainties for the sl free energies, surface tensions, adhesion works, and solvation free energies are ± 2 meV/Å^2. The entropy uncertainty for the sl system is $\pm$ 0.01 meV/K.

Surface	γ_{sv}	S_{H_2O}	$\gamma_{sl}(E)$	$\Delta\gamma_{sl}(S)$	$\gamma_{sl}(F)$	W_{ad}	F_{solv}	θ_{sl}
Pd	61.37	0.64	56.0	11.49	44.52	21.31	−16.85	0
Pt	86.99	0.56	72.57	1.60	70.96	20.49	−16.03	0
Rh	103.80	0.59	96.28	2.62	93.65	14.61	−10.15	0
Pd-Au	47.72	0.61	42.29	4.67	42.61	9.56	−5.10	0
Ag	36.96	0.60	39.37	5.18	34.19	7.23	−2.77	52
Au	33.91	0.59	36.62	2.31	34.31	4.06	+0.40	95

TABLE II. Local entropies in meV/K per water molecule for 1WL and IBL. The entropy of liquid bulk water is 0.55 meV/K. The entropy uncertainty is $\pm$ 0.01 meV/K.

S_{H_2O}	Au	Ag	Pd-Au	Pt	Rh	Pd
1WL	0.75	0.77	0.56	0.59	0.70	0.68
IBL	0.66	0.64	0.64	0.61	0.58	0.67

have the lowest 1WL entropies close to the bulk value. On Pt, both the 1WL and IBL entropies are similar and small, which can be understood by the high water diffusion barrier on the surface[89] and the relatively structured, rigid interfacial water. Rh has a large 1WL and the smallest IBL contribution, which can be understood by the facile water diffusion[89] in the 1WL despite the very structured water in this region. The highest IBL entropies are found for Pd and Au. Since the number of water molecules in the IBL region is significantly higher than in the 1WL, IBL dominates the sl interface formation entropy. It appears that the highly exergonic solvation of Pd is a result of a modest water adsorption strength and high IBL entropic contributions.

The total water entropy also correlates strongly with the orientational water density in Figure 3. In particular, the highest entropy contributions are observed for interfaces with a moderately ordered first water layer. For instance, Pd and Ag have the highest entropy contributions $\Delta\gamma_{sl}$, and they also have a moderately organized water layer. Pt and Rh, on the other hand, have low entropy contributions and highly ordered water layers, while Au has weakly ordered water and modest entropy contributions.

Having identified the correlation between the order of the water layers and their entropy, it is still surprising that all computed local entropies of the considered interfacial water layers are higher than those of bulk water. Naively one would expect that the entropy of the interfacial water molecules is lower than the one of bulk liquid water molecules. However, recent experimental studies[91,92] of two-dimensional water layers on a porous hydrophilic silica glass surface estimated that the entropy of these 2D water layers should be twice the one of bulk water. They attributed this high entropy to the fact that due to the two-dimensional topology the ideal tetrahedral bulk water symmetry can hardly be realized in two-dimensional water. This argument might well also be valid in the interfacial systems considered in our study. The higher entropy of interfacial water has also been observed in simulations of graphitic carbon surfaces, where the increased entropy was attributed to destabilization of the interfacial hydrogen bond network which in turn increases the low-frequency translational and librational DoS.[48]

Besides entropy, also the adsorption energy of a single water molecule exhibits strong correlations with the water density and orientational density. The comparison of Figure 3 and 7 show that the most ordered interfacial water structures are observed for the surfaces with the strongest water molecule adsorption. The more structured interfacial water layer and stronger adsorption energy also lead to more oscillatory electrostatic potential profiles as shown in Figure S2.

When analyzing the interfacial entropies, it should also be noted that in our computational model the interfacial water molecules are rather free to move in the z-coordinate due to the presence of the vacuum layer. The water molecules may eventually drift into the vacuum, but they are captured back into the water layer again for the duration of the simulation. While we have corrected for the formation and solvation free energies by removing the γ_{lv}-term, the free relaxation of the water film does not guarantee a fixed bulk density of 1 g/cm^3 corresponding to standard pressure conditions. As a result, the volume of the water film tends to fluctuate and the average bulk density becomes lower than 1 g/cm^3.[61] The lower density leads to somewhat higher entropies as can be inferred from experimental data, showing that increasing the water temperature by 25 K decreases water density by ca. 1 % but increases the entropy by 0.06 meV/K from 0.65 to 0.79 meV/K.[79] Therefore, the larger entropy of water in the IBL region, as shown in Table II, may at least partially be due to the lower density of water in the simulations. Nevertheless, the effect of the lower water entropy on the (computed) total entropy is modest compared to the experiment.

IV. DISCUSSION

Our work highlights the complex interplay between entropy and internal energy in the formation of metal–water interfaces. We have shown that while the water adsorption energy is a good descriptor of the internal energy part of the interface formation, it alone cannot satisfactorily explain the interfacial thermodynamics due to the notable and metal-dependent entropic contributions of water at room temperature. Our results show that the metal-water interface formation is entropically most favorable for surfaces with a moderately organized water structure and a high number of translational degrees of freedom at low frequencies. Combined together, the most favorable surface solvation is observed for Pd, which forms a moderately strong bond with water but still has a fairly flexible interfacial water layer.

It appears that the interface formation is driven by the competition or compensation between entropy and internal energy. While these compensation effects have not been discussed in the context of metal–water interface thermodynamics, these concepts are well established in biophysics.[93–95] While the full mechanistic details behind the entropy–energy compensation are still debated, it is clear that the low-frequency vibrations and slow water dynamics significantly contribute to the entropy.[93] While strong interactions such as hydrogen bonding or adsorption lead to favorable energetic contributions, they slow water reorganization and lower entropy.

Our results can also be contrasted with the previous analytic theories of solid–liquid interface thermodynamics. For example, Berry's simple breaking-bonds model assumes that the work of adhesion and contact angle are proportional to the product of the liquid binding energy and the liquid interfacial density.[96,97] While this model satisfactorily predicts the internal energy contributions, it cannot model the entropic effects and free energy, and is therefore not applicable for predicting metal–water interfacial thermodynamics. The more refined models show that the interfacial thermodynamics are not dictated only by the interfacial density and the interaction strength, but also depend on the one- and two-body correlation functions as well as on the delicate balance between liquid-liquid and solid-liquid interaction strengths.[96,98–100] While the resulting integral-differential equations of the correlation functions are too complex to be solved for water, these models highlight that solid–liquid thermodynamics are not determined by the adsorption energy alone, but depend on the liquid structure, the interaction strengths or internal energies, and the entropy as we have also highlighted herein.

Following the logic of analytic surface tension models, we have also linked the water structure with its interfacial thermodynamic properties. We have, for instance, shown that the more structured or ordered interfacial water layers (Figure 3) correspond to smaller interfacial entropy contributions. As we have discussed in relation to Figure 3, the higher interfacial water entropies are observed on Ag and Pd which feature a modestly ordered water layer while smaller entropies correspond to either highly organized (Pt and Rh) or weakly ordered water (Au). Detailed entropy analysis also shows that the interfacial water layers have higher entropy than bulk water, probably due a disrupted hydrogen bonding network and the increased population of low-frequency translational water modes. Therefore, it is not enough to focus on the structure because the entropy arises mainly from the low-frequency modes of translation and rotation so consideration of water dynamics is crucial.

Besides the fundamental understanding of interfacial structure and thermodynamics, the results of this work can be used for validating, benchmarking, and parameterizing other simulation methods. For instance, the contact angles and water structures we have obtained using DFT-MD differ significantly from those by Gim *et al.*[14] who employed QM/MM-MD. The interfacial water entropies computed in our work for Pt differ from those obtained by Jung *et al.*[84], who used ReaxFF-MD. In particular, the interfacial water entropies by Jung are about 30 % smaller than ours. We speculate that the differences are due to both the short sampling time (1.5 ps) in the PT2 simulations and the deficiencies of the ReaxFF force field parameterized for Pt-O rather than Pt-H_2O systems. These comparisons underscore the importance of QM/MM and ReaxFF validation and parameterization against DFT-MD quality data. We also anticipate that the results herein provide a rigorous test for current and future machine learning interatomic potentials.

In addition to explicit solvent methods, the present data can also be applied to benchmarking and developing implicit solvent methods at different levels of theory, ranging from classical density functional and integral equation theories to dielectric continuum solvent models. For instance, even the minimal parameterization of dielectric continuum models requires at least structural and thermodynamic data for the cavity function and the effective interaction free energy, respectively.[34] Up until now, the needed data has been available only for small molecules and ions, and even when continuum models are applied to modelling metallic surfaces, the parameter sets developed for molecules and ions in bulk liquids are utilized due to the lack of metal-specific structural and thermodynamic data; this is very problematic as the implicit solvent models require system-dependent parameterization. As the needed free energies of surface solvation have not been measured for well-defined surfaces, the best option is to utilize computed values. Hence, the current work presents the first step towards a reliable computation of thermodynamic and structural data, which can be used in parameterizing and benchmarking metal–water-specific implicit solvent models.

Finally, the applicability of the used DFT-MD + 2PT methodology is not limited to metal–water interfaces only. Some applications relevant to electrocatalysis, electrochemistry, and materials science include the study of pH and electrolyte effects on the interfacial liquid thermodynamics and structure. While studying such systems might necessitate longer simulation timescales or the use of more sophisticated functionals, the computational approach itself is very general and reasonably efficient for large-scale DFT-MD studies.

V. CONCLUSIONS

We have addressed the thermodynamics of solid–liquid interface formation through extensive DFT-MD simulations and detailed entropy analyses within the 2PT formalism. Through this approach, we were able to several thermodynamic quantities, such as free energies, entropies, adhesion works, and surface tensions for a range of relevant metal–water interfaces (FCC(111) Pt, Pd, Au, Ag, Rh, and AuPd) for the first time to our knowledge. To understand the atomistic origins of these thermodynamic quantities, we have correlated them with both structural and energetic quantities.

Overall, our study provides detailed fundamental information on the formation of metal–water interfaces encountered in several applications in electrochemistry, catalysis, and materials science. Our results show that the interface formation is driven by both energetic and entropic contributions. For the most strongly binding metals, Pt and Rh, the water adsorption energy dominates the formation thermodynamics while on slightly less binding metals, Pd and Ag, both entropic and energetic contributions are sizable. Our results also show that both highly structured (Rh and Pt) and unstructured (Au) interfacial water layers lead to small interfacial entropy contributions while the highest interfacial water entropies are observed for modestly ordered water layers (Ag and Pd). The entropy analysis shows that interfacial water has higher entropy than bulk water. The obtained results show that metal–water interface formation thermodynamics cannot be described using adsorption energies and the water structures alone because entropy arises mainly from the *dynamics* of the low frequency modes of translation and rotation.

Our work also provides the first concise DFT-MD -level dataset for interfacial metal–water thermodynamics, which will be highly valuable for experimental, theoretical, and computational developments. First, we anticipate that our study motivates the experimental determination of solid–liquid thermodynamics for a range of systems as the thermodynamics can aid the development and design of, e.g., electrochemical and electrocatalytic interfaces where the surface wettability is of primary interest. Second, the correlations identified between thermodynamics, binding energies, atomic structure, slow water dynamics, and entropy will hopefully aid the development of improved implicit solvent models at different levels of theory. Finally, the results from this work can be directly used to benchmark and parameterize classical explicit and implicit solvent models often applied to study solvated interfaces. In particular, the obtained thermodynamic and structural data can be used for constructing surface-specific implicit solvent models to overcome the known issues of using small molecule data to parameterize dielectric continuum models for metallic interfaces.

VI. SUPPLEMENTARY MATERIAL

S1: Details on the free energy calculations, S2: Computation of interfacial entropies, S3: The bending and stretching mode DoS for interfacial and bulk water, S4: Electrostatic potential profiles, S5: Comparison of translational and rotational DOSs, S6: Convergence and uncertainty analysis, S7: Potentials of zero charge

VII. ACKNOWLEDGEMENTS

M.M.M. and F.D.-F. acknowledge the funding by the Academy of Finland (projects #307853 and #338228). A.G. and S.S. acknowledge the support by the Dr. Barbara Mez-Starck Foundation. The computational resources were provided by the state of Baden-Württemberg through bwHPC and the German Research Foundation (DFG) under grant no INST 40/575-1 FUGG (JUSTUS 2 cluster), by CSC - IT CENTER FOR SCIENCE LTD, and the FGCI - Finnish Grid and Cloud Infrastructure. M.M.M. also thanks and acknowledges Prof. Jun Huang for helpful discussions on and providing references for the experimental entropy measurements.

VIII. CONFLICT OF INTEREST STATEMENT

The authors have no conflicts to disclose.

IX. AUTHOR CONTRIBUTIONS

F.D.-F.: Data Curation (equal), Formal Analysis (equal), Visualization (equal), Validation (equal), Original Draft Preparation (equal), Writing/Review & Editing (equal).

T.K.: Data Curation (equal), Formal Analysis (equal), Original Draft Preparation (equal), Writing/Review & Editing (equal), Supervision (equal), Validation (equal), Methodology (equal).

A.G.: Writing/Review & Editing (equal), Supervision (supporting), Resources (equal), Funding Acquisition (lead).

S.S.: Data Curation (equal), Formal Analysis (equal), Software (lead), Visualization (equal), Original Draft Preparation (supporting), Writing/Review & Editing (equal), Supervision (supporting), Validation (equal), Methodology (equal), Resources (supporting), Project Administration (supporting).

M.M.M.: Conceptualization (lead), Formal Analysis (equal), Writing/Original Draft Preparation (lead), Writing/Review & Editing (equal), Supervision (lead), Validation (equal), Methodology (equal), Resources (lead), Project Administration (lead), Funding Acquisition (lead).

X. DATA AVAILABILITY

All original data, trajectories, and Excel sheets are openly shared through the Etsin fairdata service with DOI `https://doi.org/10.23729/f700b740-e5a3-4c6c-a636-2d52b74b99b5`.

[1] O. Gerard, A. Numan, S. Krishnan, M. Khalid, R. Subramaniam, and R. Kasi, "A review on the recent advances in binder-free electrodes for electrochemical energy storage application," Journal of Energy Storage **50**, 104283 (2022).

[2]R. W. Haid, X. Ding, T. K. Sarpey, A. S. Bandarenka, and B. Garlyyev, "Exploration of the electrical double-layer structure: Influence of electrolyte components on the double-layer capacitance and potential of maximum entropy," Current Opinion in Electrochemistry **32**, 100882 (2022).
[3]G. Gonella, E. H. G. Backus, Y. Nagata, D. J. Bonthuis, P. Loche, A. Schlaich, R. R. Netz, A. Kühnle, I. T. McCrum, M. T. M. Koper, M. Wolf, B. Winter, G. Meijer, R. K. Campen, and M. Bonn, "Water at charged interfaces," Nature Reviews Chemistry **5**, 466–485 (2021).
[4]O. Björneholm, M. H. Hansen, A. Hodgson, L.-M. Liu, D. T. Limmer, A. Michaelides, P. Pedevilla, J. Rossmeisl, H. Shen, G. Tocci, E. Tyrode, M.-M. Walz, J. Werner, and H. Bluhm, "Water at interfaces," Chemical Reviews **116**, 7698–7726 (2016).
[5]A. Groß and S. Sakong, "Ab initio simulations of water/metal interfaces," Chemical Reviews **122**, 10746–10776 (2022).
[6]S. Ringe, "Cation effects on electrocatalytic reduction processes at the example of the hydrogen evolution reaction," Current Opinion in Electrochemistry **39**, 101268 (2023).
[7]M. T. M. Koper, A. Z. Weber, K. Chan, and J. Cheng, "Introduction: Computational electrochemistry," Chemical Reviews **122**, 10579–10580 (2022).
[8]F. Domínguez-Flores and M. M. Melander, "Electrocatalytic rate constants from dft simulations and theoretical models: Learning from each other," Current Opinion in Electrochemistry **36**, 101110 (2022).
[9]O. M. Magnussen and A. Gross, "Toward an atomic-scale understanding of electrochemical interface structure and dynamics," Journal of the American Chemical Society **141**, 4777–4790 (2019).
[10]J. Carrasco, A. Hodgson, and A. Michaelides, "A molecular perspective of water at metal interfaces," Nature Materials **11**, 667–674 (2012).
[11]K. Shi, Z. Ren, Z. Meng, and X. Feng, "Hydrophilic or hydrophobic? Optimizing the catalyst microenvironment for gas-involving electrocatalysis," ChemCatChem **16**, e202301308 (2024).
[12]N. Oliveira and Y. Yan, "Interfacial water structural entropy as the descriptor for ph-dependent hor/her activity on pt," ChemRxiv (2024), 10.26434/chemrxiv-2024-wsjwh.
[13]A. Hodgson and S. Haq, "Water adsorption and the wetting of metal surfaces," Surface Science Reports **64**, 381–451 (2009).
[14]S. Gim, K. J. Cho, H.-K. Lim, and H. Kim, "Structure, dynamics, and wettability of water at metal interfaces," Scientific Reports **9**, 14805 (2019).
[15]J. Rafiee, X. Mi, H. Gullapalli, A. V. Thomas, F. Yavari, Y. Shi, P. M. Ajayan, and N. A. Koratkar, "Wetting transparency of graphene," Nature Materials **11**, 217–222 (2012).
[16]J. Bico, C. Marzolin, and D. Quéré, "Pearl drops," Europhysics Letters **47**, 220 (1999).
[17]D. J. Trevoy and H. J. Johnson, "The water wettability of metal surfaces," The Journal of Physical Chemistry **62**, 833–837 (1958).
[18]M. A. Osman and B. A. Keller, "Wettability of native silver surfaces," Applied Surface Science **99**, 261–263 (1996).
[19]M. E. Schrader, "Wettability of clean metal surfaces," Journal of Colloid and Interface Science **100**, 372–380 (1984).
[20]L. Somlyai-Sipos and P. Baumli, "Wettability of metals by water," Metals **12** (2022).
[21]Y. Zhang, S. E. Feller, B. R. Brooks, and R. W. Pastor, "Computer simulation of liquid/liquid interfaces. i. theory and application to octane/water," The Journal of Chemical Physics **103**, 10252–10266 (1995), https://doi.org/10.1063/1.469927.
[22]K. W. Bewig and W. A. Zisman, "The wetting of gold and platinum by water," The Journal of Physical Chemistry **69**, 4238–4242 (1965).
[23]M. E. Schrader, "Ultrahigh-vacuum techniques in the measurement of contact angles. II. Water on gold," The Journal of Physical Chemistry **74**, 2313–2317 (1970).
[24]J. Ma, I. Zarin, and N. Miljkovic, "Direct measurement of solid-liquid interfacial energy using a meniscus," Phys. Rev. Lett. **129**, 246802 (2022).
[25]J. Harrison, J. Randles, and D. Schiffrin, "The entropy of formation of the mercury-aqueous solution interface and the structure of the inner layer," Journal of Electroanalytical Chemistry and Interfacial Electrochemistry **48**, 359–381 (1973).
[26]G. Hills and S. Hsieh, "Surface excess entropies and volumes of the mercury-electrolyte interface," Journal of Electroanalytical Chemistry and Interfacial Electrochemistry **58**, 289–298 (1975).
[27]S. Trasatti, "Structure of the metal/electrolyte solution interface: new data for theory," Electrochimica Acta **36**, 1659–1667 (1991).
[28]R. Guidelli, G. Aloisi, E. Leiva, and W. Schmickler, "Contribution to the entropy of formation of metal/solution interphases from metal electrons," The Journal of Physical Chemistry **92**, 6671–6675 (1988).
[29]F. Silva, M. J. Sottomayor, and A. Martins, "Temperature coefficient of the potential of zero charge and entropies of formation for the interface of stepped faces of gold in contact with aqueous perchloric acid solutions," J. Chem. Soc., Faraday Trans. **92**, 3693–3699 (1996).
[30]F. Silva, M. Sottomayor, A. Hamelin, and L. Stoicoviciu, "The temperature dependence of double layer properties of gold faces in perchloric acid: Part III. the gold (100) face," Journal of Electroanalytical Chemistry and Interfacial Electrochemistry **295**, 301–316 (1990).
[31]A. Gross and S. Sakong, "Modelling the electric double layer at electrode/electrolyte interfaces," Current Opinion in Electrochemistry **14**, 1 – 6 (2019).
[32]G. Jeanmairet, B. Rotenberg, and M. Salanne, "Microscopic simulations of electrochemical double-layer capacitors," Chemical Reviews **122**, 10860–10898 (2022).
[33]M. Becker, P. Loche, M. Rezaei, A. Wolde-Kidan, Y. Uematsu, R. R. Netz, and D. J. Bonthuis, "Multiscale modeling of aqueous electric double layers," Chemical Reviews **124**, 1–26 (2024).
[34]S. Ringe, N. G. Hörmann, H. Oberhofer, and K. Reuter, "Implicit solvation methods for catalysis at electrified interfaces," Chem. Rev. **122**, 10777–10820 (2022).
[35]J.-P. Hansen and I. R. McDonald, *Theory of Simple Liquids, 3rd Edition* (Academic Press, 2006).
[36]A. M. Maldonado, S. Hagiwara, T. H. Choi, F. Eckert, K. Schwarz, R. Sundararaman, M. Otani, and J. A. Keith, "Quantifying uncertainties in solvation procedures for modeling aqueous phase reaction mechanisms," The Journal of Physical Chemistry A **125**, 154–164 (2021).
[37]S. Hagiwara, S. Nishihara, F. Kuroda, and M. Otani, "Development of a dielectrically consistent reference interaction site model combined with the density functional theory for electrochemical interface simulations," Phys. Rev. Mater. **6**, 093802 (2022).
[38]M. Lbadaoui-Darvas, G. Garberoglio, K. S. Karadima, M. N. D. S. Cordeiro, A. Nenes, and S. Takahama, "Molecular simulations of interfacial systems: challenges, applications and future perspectives," Molecular Simulation **49**, 1229–1266 (2023).
[39]G. J. Gloor, G. Jackson, F. J. Blas, and E. de Miguel, "Test-area simulation method for the direct determination of the interfacial tension of systems with continuous or discontinuous potentials," The Journal of Chemical Physics **123**, 134703 (2005).
[40]E. Salomons and M. Mareschal, "Surface tension, adsorption and surface entropy of liquid-vapour systems by atomistic simulation," Journal of Physics: Condensed Matter **3**, 3645 (1991).
[41]H. Jiang and A. J. Patel, "Recent advances in estimating contact angles using molecular simulations and enhanced sampling methods," Current Opinion in Chemical Engineering **23**, 130–137 (2019).
[42]T. Dreher, C. Lemarchand, L. Soulard, E. Bourasseau, P. Malfreyt, and N. Pineau, "Calculation of a solid/liquid surface tension: A methodological study," The Journal of Chemical Physics **148**, 034702 (2018).
[43]X. Qi, Y. Zhou, and K. A. Fichthorn, "Obtaining the solid-liquid interfacial free energy via multi-scheme thermodynamic integration: Ag-ethylene glycol interfaces," The Journal of Chemical Physics **145**, 194108 (2016).
[44]F. Leroy, D. J. V. A. dos Santos, and F. Müller-Plathe, "Interfacial excess free energies of solid–liquid interfaces by molecular dynamics simulation and thermodynamic integration," Macromolecular Rapid Communications **30**, 864–870 (2009).
[45]R. Jinnouchi, F. Karsai, C. Verdi, and G. Kresse, "First-principles hydration free energies of oxygenated species at water–platinum interfaces," The Journal of Chemical Physics **154**, 094107 (2021).
[46]S.-T. Lin, P. K. Maiti, and W. A. I. Goddard, "Two-phase thermodynamic model for efficient and accurate absolute entropy of water from molecular dynamics simulations," The Journal of Physical Chemistry B **114**, 8191–8198 (2010), https://doi.org/10.1021/jp103120q.
[47]P. H. Berens, D. H. J. Mackay, G. M. White, and K. R. Wilson, "Thermodynamics and quantum corrections from molecular dynamics for liquid water," The Journal of Chemical Physics **79**, 2375–2389 (1983),

https://doi.org/10.1063/1.446044.
[48]T. A. Pascal, S.-T. Lin, and W. A. Goddard III, "Thermodynamics of liquids: standard molar entropies and heat capacities of common solvents from 2PT molecular dynamics," Phys. Chem. Chem. Phys. **13**, 169–181 (2011).
[49]S.-T. Lin, M. Blanco, and W. A. Goddard, "The two-phase model for calculating thermodynamic properties of liquids from molecular dynamics: Validation for the phase diagram of lennard-jones fluids," The Journal of Chemical Physics **119**, 11792–11805 (2003).
[50]J.-B. Le and J. Cheng, "Modeling electrochemical interfaces from ab initio molecular dynamics: water adsorption on metal surfaces at potential of zero charge," Current Opinion in Electrochemistry **19**, 129 – 136 (2020), fundamental and Theoretical Electrochemistry Bioelectrochemistry.
[51]J. Le, A. Cuesta, and J. Cheng, "The structure of metal-water interface at the potential of zero charge from density functional theory-based molecular dynamics," Journal of Electroanalytical Chemistry **819**, 87 – 94 (2018).
[52]J. Le, M. Iannuzzi, A. Cuesta, and J. Cheng, "Determining potentials of zero charge of metal electrodes versus the standard hydrogen electrode from density-functional-theory-based molecular dynamics," Phys. Rev. Lett. **119**, 016801 (2017).
[53]P. Li, J. Huang, Y. Hu, and S. Chen, "Establishment of the potential of zero charge of metals in aqueous solutions: Different faces of water revealed by ab initio molecular dynamics simulations," The Journal of Physical Chemistry C **125**, 3972–3979 (2021).
[54]L. Li, Y.-P. Liu, J.-B. Le, and J. Cheng, "Unraveling molecular structures and ion effects of electric double layers at metal water interfaces," Cell Reports Physical Science **3**, 100759 (2022).
[55]S. Sakong and A. Groß, "The electric double layer at metal-water interfaces revisited based on a charge polarization scheme," J. Chem. Phys. **149**, 084705 (2018).
[56]S. Sakong and A. Groß, "Water structures on a Pt(111) electrode from ab initio molecular dynamic simulations for a variety of electrochemical conditions," Phys. Chem. Chem. Phys. **22**, 10431–10437 (2020).
[57]S. Gim, H.-K. Lim, and H. Kim, "Multiscale simulation method for quantitative prediction of surface wettability at the atomistic level," The Journal of Physical Chemistry Letters **9**, 1750–1758 (2018), https://doi.org/10.1021/acs.jpclett.8b00466.
[58]P. Clabaut, R. Staub, J. Galiana, E. Antonetti, and S. N. Steinmann, "Water adlayers on noble metal surfaces: Insights from energy decomposition analysis," The Journal of Chemical Physics **153**, 054703 (2020).
[59]P. Clabaut, P. Fleurat-Lessard, C. Michel, and S. N. Steinmann, "Ten facets, one force field: The GAL19 force field for water–noble metal interfaces," Journal of Chemical Theory and Computation **16**, 4565–4578 (2020).
[60]C.-Y. Li, J.-B. Le, Y.-H. Wang, S. Chen, Z.-L. Yang, J.-F. Li, J. Cheng, and Z.-Q. Tian, "In situ probing electrified interfacial water structures at atomically flat surfaces ," Nature Materials **18**, 697–701 (2019).
[61]S. Sakong, K. Forster-Tonigold, and A. Groß, "The structure of water at a Pt(111) electrode and the potential of zero charge studied from first principles," The Journal of Chemical Physics **144** (2016), 10.1063/1.4948638.
[62]G. Kresse and J. Hafner, "Ab initio molecular dynamics for liquid metals," Phys. Rev. B **47**, 558–561 (1993).
[63]G. Kresse and J. Furthmüller, "Efficiency of ab-initio total energy calculations for metals and semiconductors using a plane-wave basis set," Computational Materials Science **6**, 15–50 (1996).
[64]G. Kresse and J. Furthmüller, "Efficient iterative schemes for ab initio total-energy calculations using a plane-wave basis set," Phys. Rev. B **54**, 11169–11186 (1996).
[65]G. Kresse and D. Joubert, "From ultrasoft pseudopotentials to the projector augmented-wave method," Phys. Rev. B **59**, 1758–1775 (1999).
[66]P. E. Blöchl, "Projector augmented-wave method," Phys. Rev. B **50**, 17953–17979 (1994).
[67]M. Xu, S. Liu, S. Vijay, T. Bligaard, and G. Kastlunger, "Benchmarking water adsorption on metal surfaces with ab-initio molecular dynamics," ChemRxiv (2024), 10.26434/chemrxiv-2024-p3qc0.
[68]K. Tonigold and A. Groß, "Dispersive interactions in water bilayers at metallic surfaces: A comparison of the pbe and rpbe functional including semiempirical dispersion corrections," Journal of Computational Chemistry **33**, 695–701 (2012).
[69]K. Forster-Tonigold and A. Groß, "Dispersion corrected RPBE studies of liquid water," The Journal of Chemical Physics **141**, 064501 (2014).
[70]B. Hammer, L. B. Hansen, and J. K. Nørskov, "Improved adsorption energetics within density-functional theory using revised perdew-burke-ernzerhof functionals," Phys. Rev. B **59**, 7413–7421 (1999).
[71]S. Grimme, J. Antony, S. Ehrlich, and H. Krieg, "A consistent and accurate ab initio parametrization of density functional dispersion correction (DFT-D) for the 94 elements H-Pu," The Journal of Chemical Physics **132**, 154104 (2010).
[72]S. Grimme, S. Ehrlich, and L. Goerigk, "Effect of the damping function in dispersion corrected density functional theory," Journal of Computational Chemistry **32**, 1456–1465 (2011).
[73]S. Sakong and A. Groß, "The importance of the electrochemical environment in the electro-oxidation of methanol on Pt(111)," ACS Catalysis **6**, 5575–5586 (2016).
[74]G. Mercurio, E. R. McNellis, I. Martin, S. Hagen, F. Leyssner, S. Soubatch, J. Meyer, M. Wolf, P. Tegeder, F. S. Tautz, and K. Reuter, "Structure and energetics of azobenzene on Ag(111): Benchmarking semiempirical dispersion correction approaches," Phys. Rev. Lett. **104**, 036102 (2010).
[75]V. Korpelin, T. Kiljunen, M. M. Melander, M. A. Caro, H. H. Kristoffersen, N. Mammen, V. Apaja, and K. Honkala, "Addressing dynamics at catalytic heterogeneous interfaces with DFT-MD: Anomalous temperature distributions from commonly used thermostats," The Journal of Physical Chemistry Letters **13**, 2644–2652 (2022).
[76]M. Paterlini and D. M. Ferguson, "Constant temperature simulations using the langevin equation with velocity verlet integration," Chemical Physics **236**, 243–252 (1998).
[77]P.-K. Lai, C.-M. Hsieh, and S.-T. Lin, "Rapid determination of entropy and free energy of mixtures from molecular dynamics simulations with the two-phase thermodynamic model," Phys. Chem. Chem. Phys. **14**, 15206–15213 (2012).
[78]P. H. Berens, D. H. J. Mackay, G. M. White, and K. R. Wilson, "Thermodynamics and quantum corrections from molecular dynamics for liquid water," The Journal of Chemical Physics **79**, 2375–2389 (1983).
[79]M. A. Caro, T. Laurila, and O. Lopez-Acevedo, "Accurate schemes for calculation of thermodynamic properties of liquid mixtures from molecular dynamics simulations," The Journal of Chemical Physics **145**, 244504 (2016).
[80]M. P. Desjarlais, "First-principles calculation of entropy for liquid metals," Phys. Rev. E **88**, 062145 (2013).
[81]S.-T. Lin, M. Blanco, and I. Goddard, William A., "The two-phase model for calculating thermodynamic properties of liquids from molecular dynamics: Validation for the phase diagram of Lennard-Jones fluids," The Journal of Chemical Physics **119**, 11792–11805 (2003).
[82]B. Kirchhoff, L. Braunwarth, C. Jung, H. Jónsson, D. Fantauzzi, and T. Jacob, "Simulations of the oxidation and degradation of platinum electrocatalysts," Small **16**, 1905159 (2020).
[83]T. A. Pascal and W. A. I. Goddard, "Entropic stabilization of water at graphitic interfaces," The Journal of Physical Chemistry Letters **12**, 9162–9168 (2021).
[84]C. K. Jung, L. Braunwarth, A. Sinyavskiy, and T. Jacob, "Thermodynamic description of interfaces applying the 2PT method on ReaxFF molecular dynamics simulations," The Journal of Physical Chemistry C **125**, 24663–24670 (2021).
[85]A. Patra, J. E. Bates, J. Sun, and J. P. Perdew, "Properties of real metallic surfaces: Effects of density functional semilocality and van der waals nonlocality," Proceedings of the National Academy of Sciences **114**, E9188–E9196 (2017).
[86]L. Vitos, A. V. Ruban, H. L. Skriver, and J. Kollár, "The surface energy of metals," Surface Science **411**, 186–202 (1998).
[87]M. F. Toney, J. N. Howard, J. Richer, G. L. Borges, J. G. Gordon, O. R. Melroy, D. G. Wiesler, D. Yee, and L. B. Sorensen, "Voltage-dependent ordering of water molecules at an electrode–electrolyte interface," Nature **368**, 444–446 (1994).
[88]S. Kim, X. Wang, J. Jang, K. Eom, S. L. Clegg, G.-S. Park, and D. Di Tommaso, "Hydrogen-bond structure and low-frequency dynamics of electrolyte solutions: Hydration numbers from ab initio water reorientation dynamics and dielectric relaxation spectroscopy," ChemPhysChem **21**, 2334–2346 (2020).

[89]W. Fang, J. Chen, P. Pedevilla, X.-Z. Li, J. O. Richardson, and A. Michaelides, "Origins of fast diffusion of water dimers on surfaces," Nature Communications **11**, 1689 (2020).
[90]L. Vitos, A. Ruban, H. Skriver, and J. Kollár, "The surface energy of metals," Surface Science **411**, 186–202 (1998).
[91]M. Bonetti and J.-M. Zanotti, "A simple AC calorimeter for specific heat measurement of liquids confined in porous materials: A study of hydrated Vycor," Review of Scientific Instruments **87**, 094903 (2016).
[92]J.-M. Zanotti, P. Judeinstein, S. Dalla-Bernardina, G. Creff, J.-B. Brubach, P. Roy, M. Bonetti, J. Ollivier, D. Sakellariou, and M.-C. Bellissent-Funel, "Competing coexisting phases in 2D water," Scientific Reports **6**, 25938 (2016).
[93]J. D. Dunitz, "Win some, lose some: enthalpy-entropy compensation in weak intermolecular interactions," Chemistry & Biology **2**, 709–712 (1995).
[94]S. Chen and Z.-G. Wang, "Using implicit-solvent potentials to extract water contributions to enthalpy–entropy compensation in biomolecular associations," The Journal of Physical Chemistry B **127**, 6825–6832 (2023).
[95]J. M. Fox, M. Zhao, M. J. Fink, K. Kang, and G. M. Whitesides, "The molecular origin of enthalpy/entropy compensation in biomolecular recognition," Annual Review of Biophysics **47**, 223–250 (2018).
[96]G. Navascues, "Liquid surfaces: theory of surface tension," Reports on Progress in Physics **42**, 1131 (1979).
[97]M. V. Berry, *Liquid surfaces* (IAEA, International Atomic Energy Agency (IAEA), 1975).
[98]G. Navascués and M. Berry, "The statistical mechanics of wetting," Molecular Physics **34**, 649–664 (1977).
[99]D. J. Diestler, "Statistical thermodynamics of the fluid-solid interface," The Journal of Physical Chemistry **100**, 10414–10422 (1996).
[100]T. Lazaridis, "Inhomogeneous fluid approach to solvation thermodynamics. 1. Theory," The Journal of Physical Chemistry B **102**, 3531–3541 (1998).